Figure S1, related to Figure1.

A

Epifluorescence Microscope Image

2 Photon Microscope Image

post-mortem histology

Mouse 2

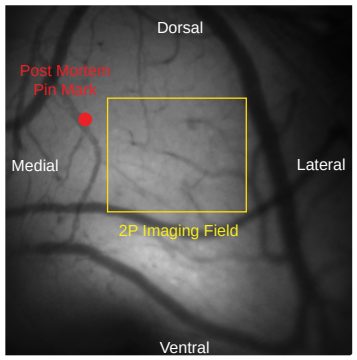

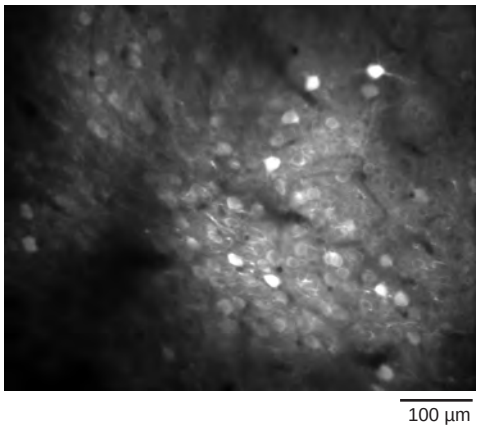

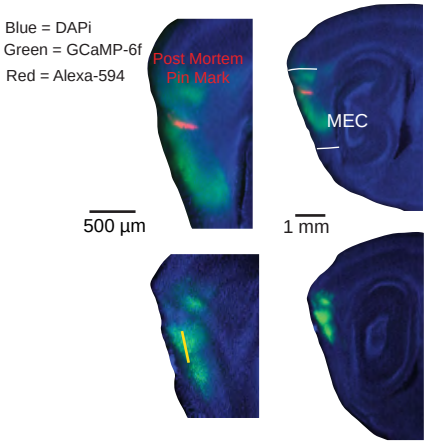

Mouse 3

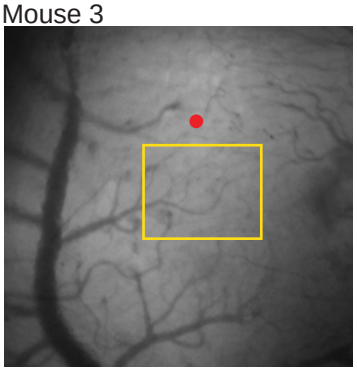

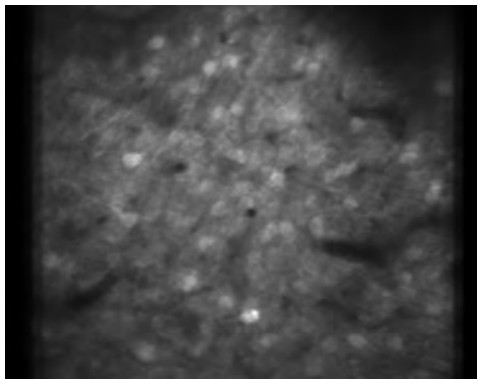

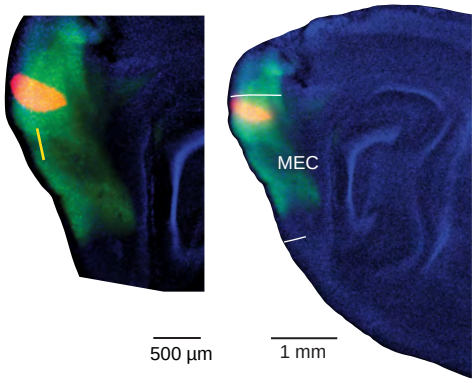

Mouse 4

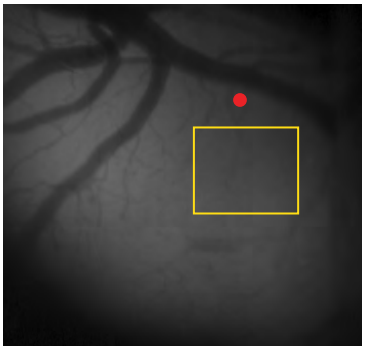

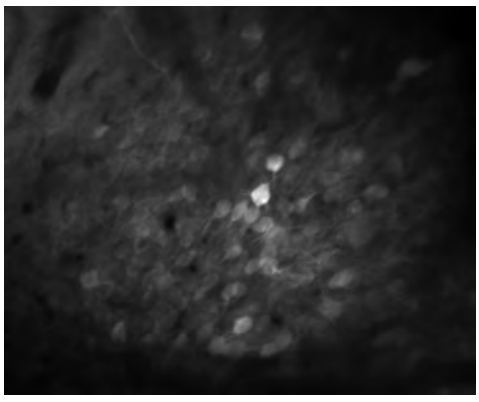

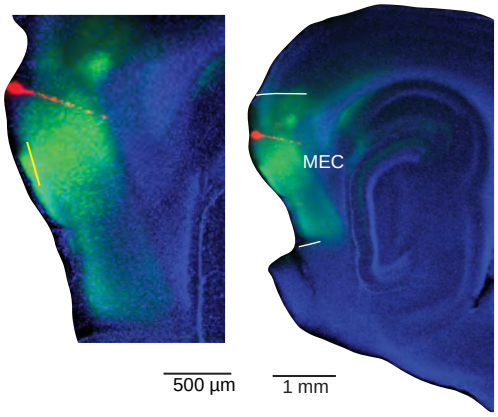

Mouse 5

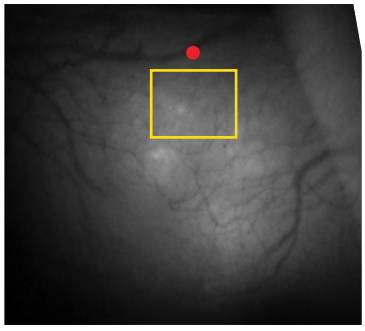

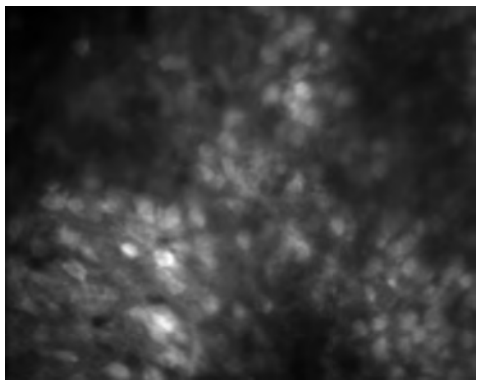

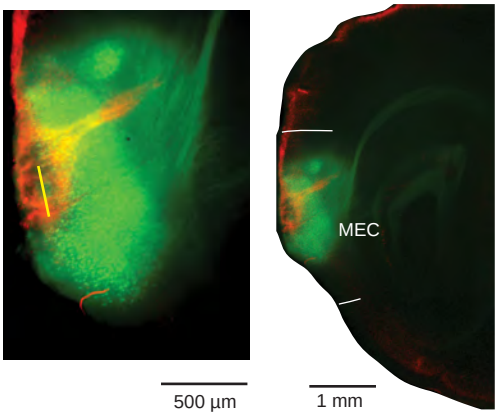

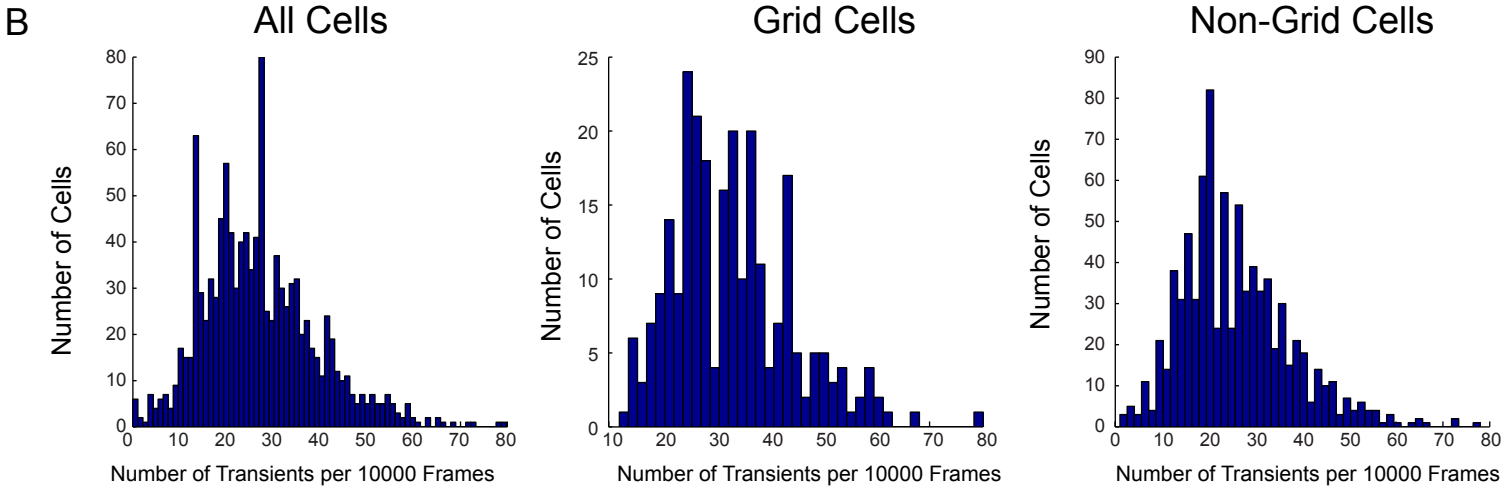
B
All Cells
Grid Cells
Non-Grid Cells
Number of Cells
Number of Transients per 10000 Frames

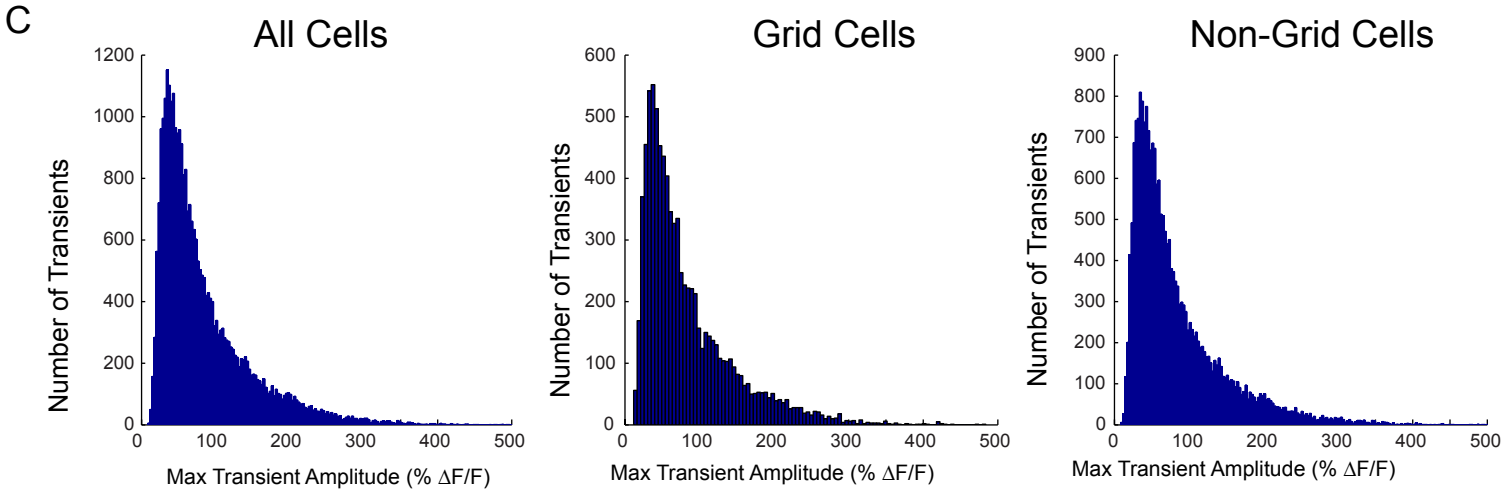
C
All Cells
Grid Cells
Non-Grid Cells
Number of Transients
Max Transient Amplitude (% ΔF/F)

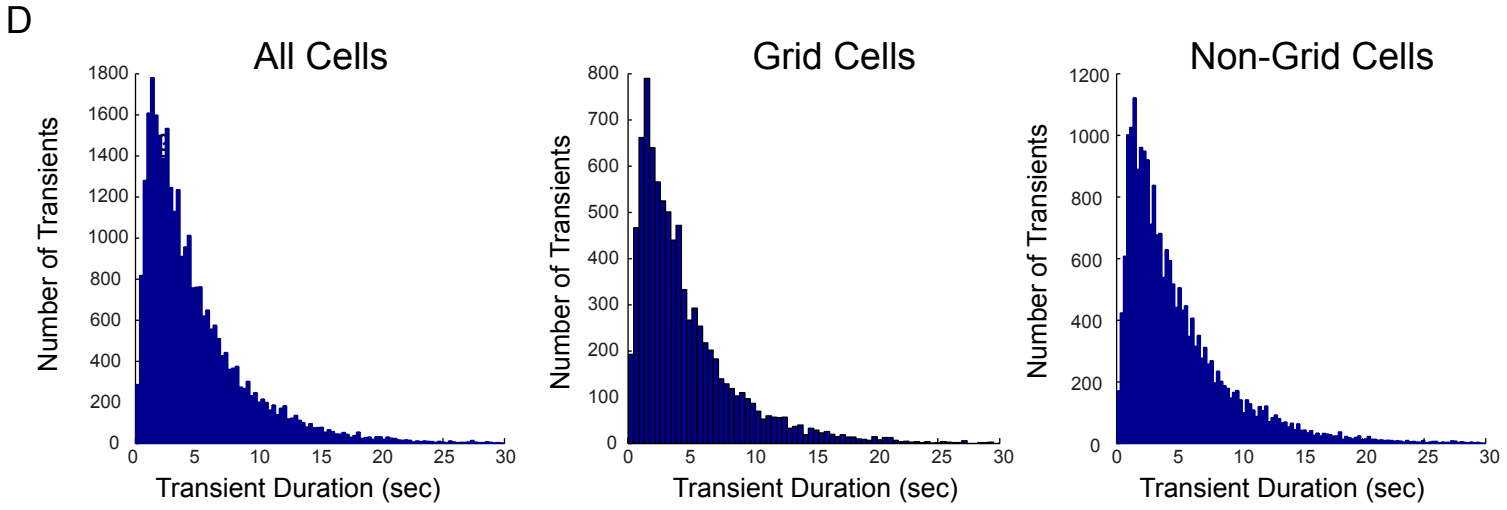
D
All Cells
Grid Cells
Non-Grid Cells
Number of Transients
Transient Duration (sec)

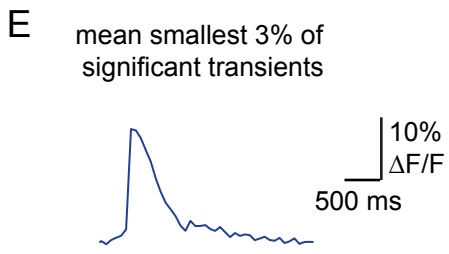
E
mean smallest 3% of
significant transients
10%
ΔF/F
500 ms

Figure S2, related to Figure 2.

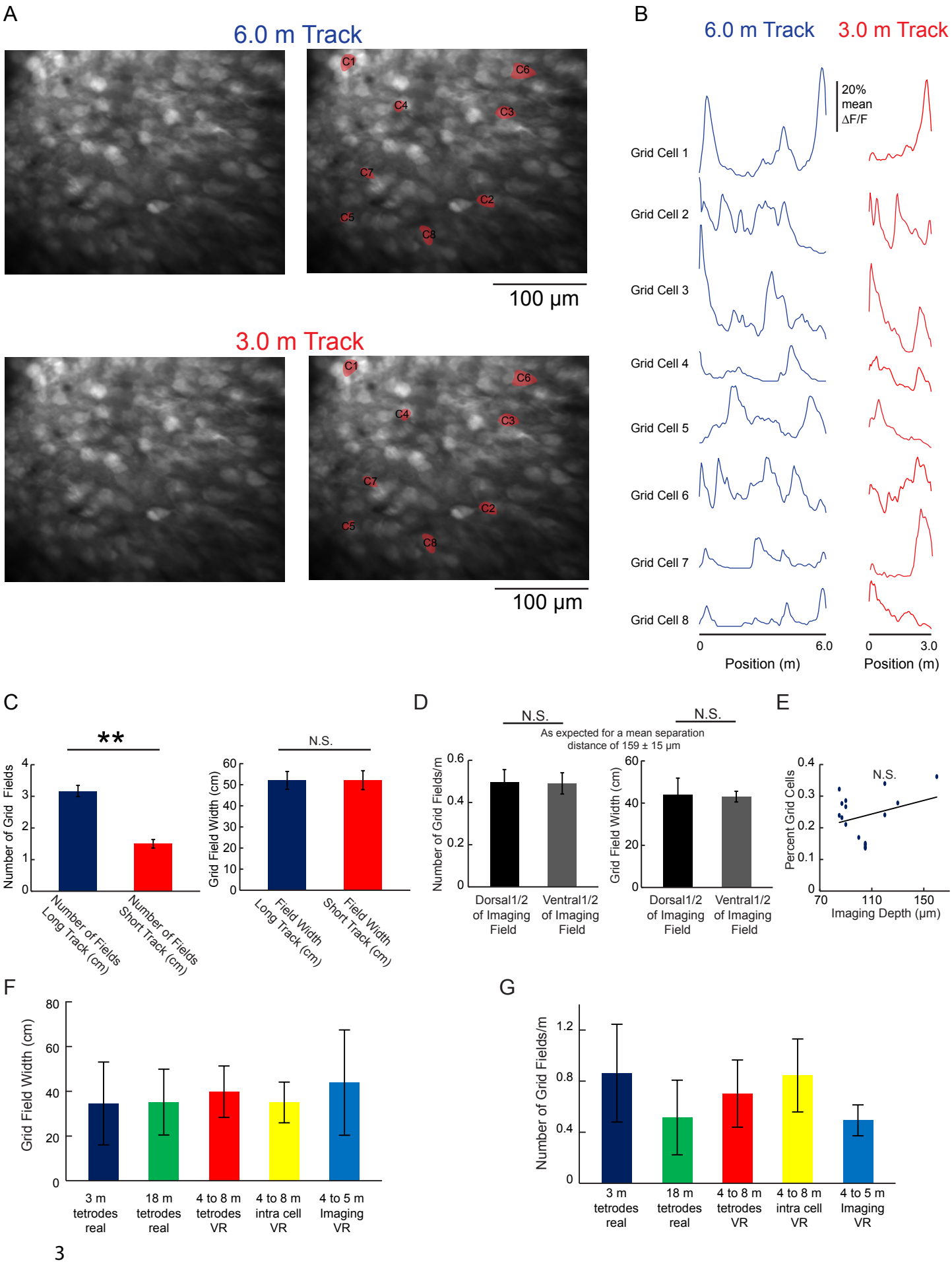

Figure S3, related to Figure 2.

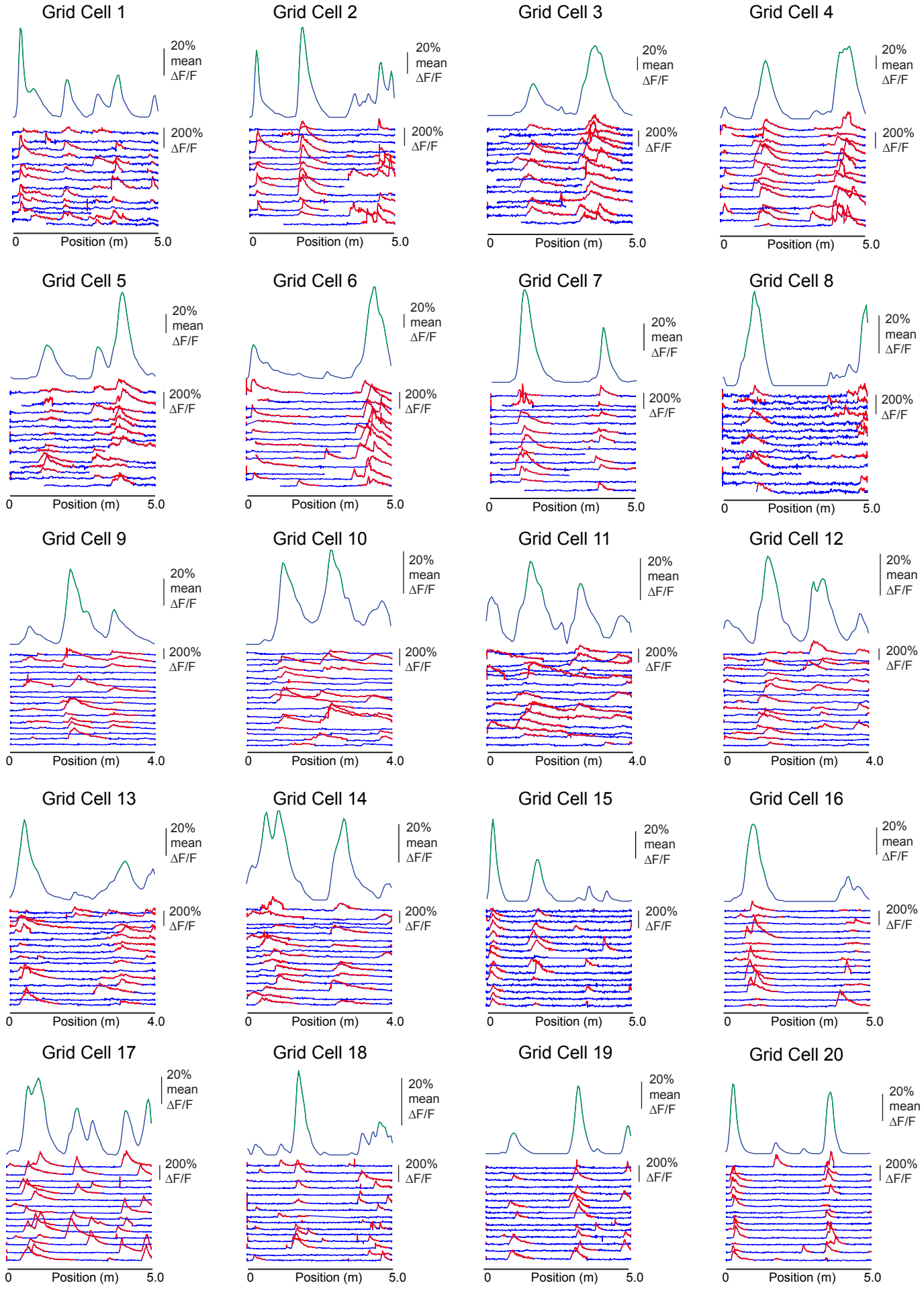

Figure S4, related to Figure 4.

A

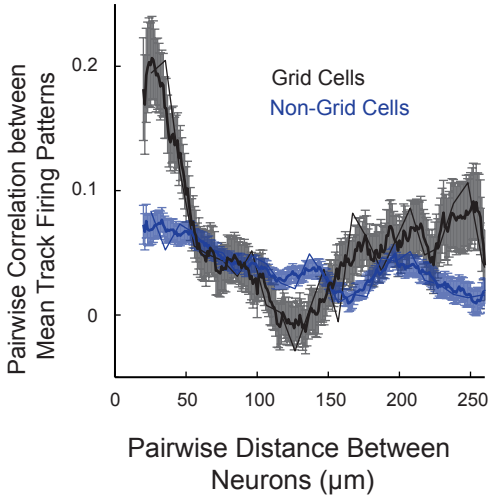

B

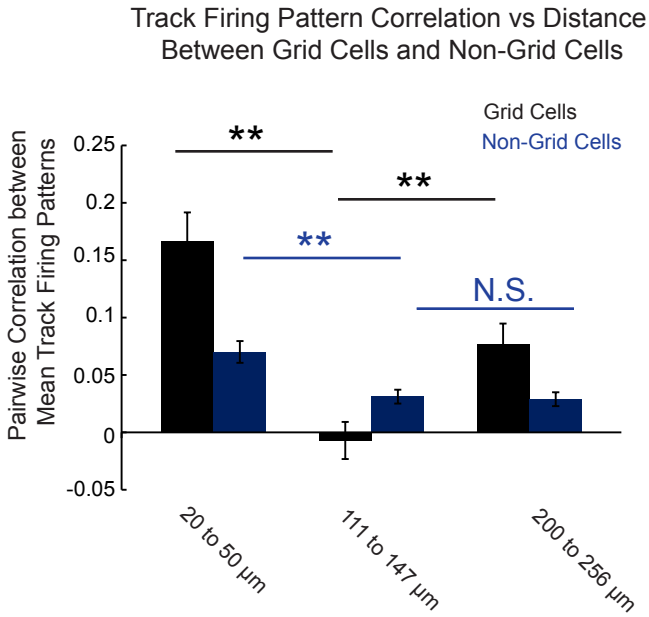

C

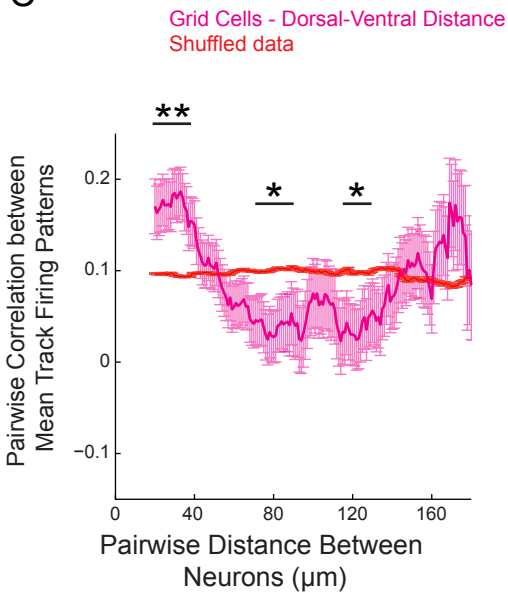

D

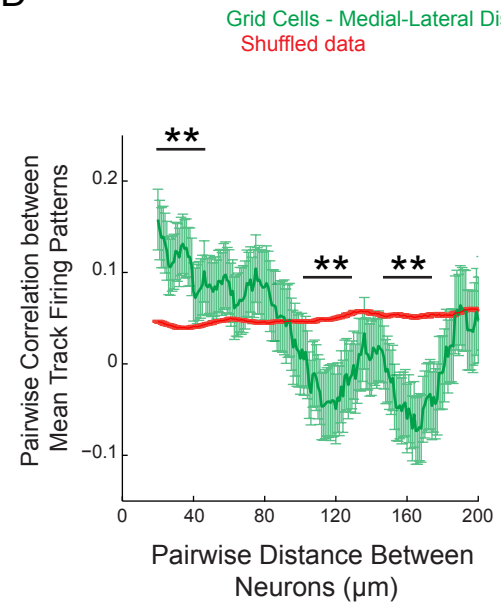

Figure S5, related to Figure 4.

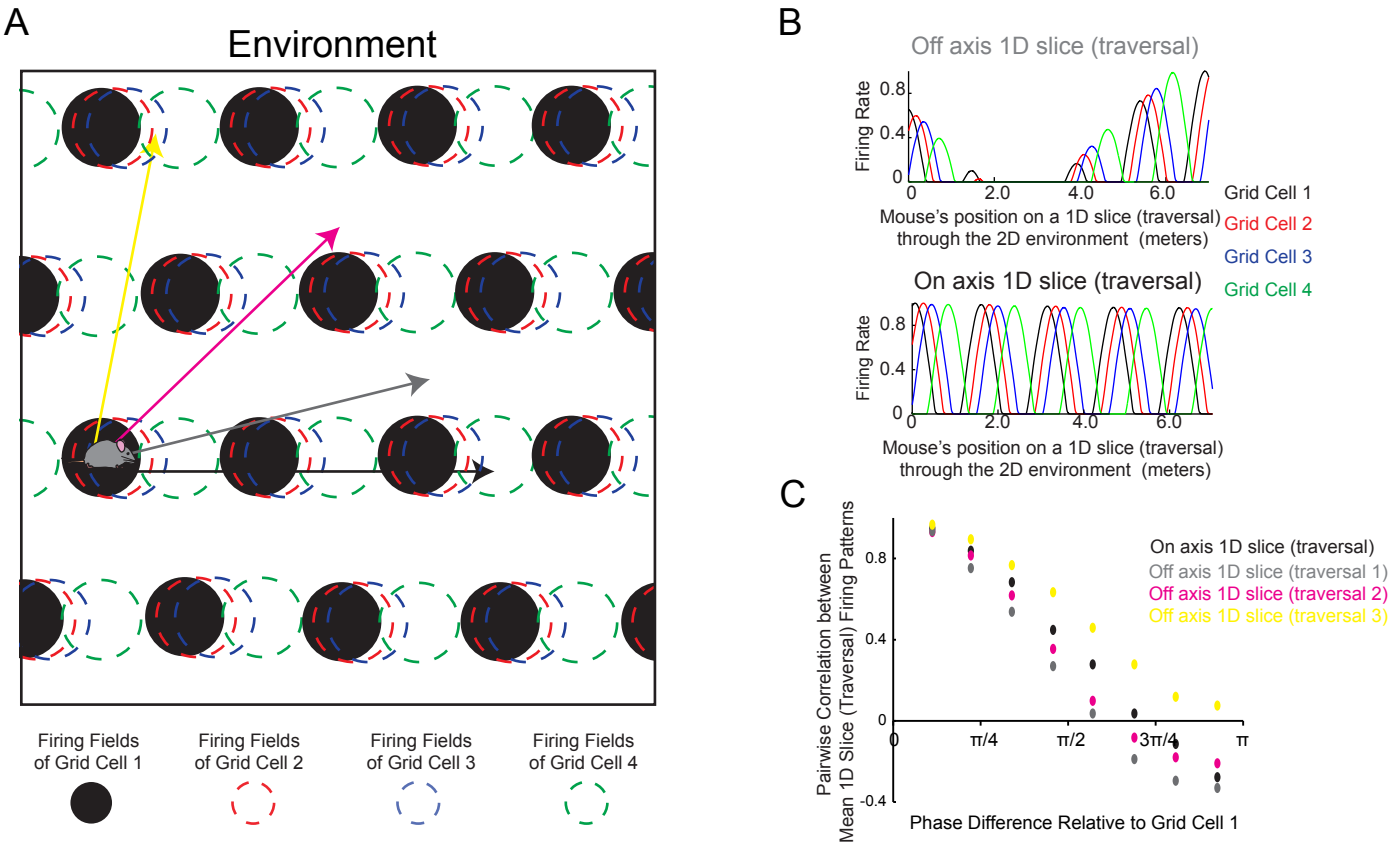

Figure S6, related to Figure 4.

A

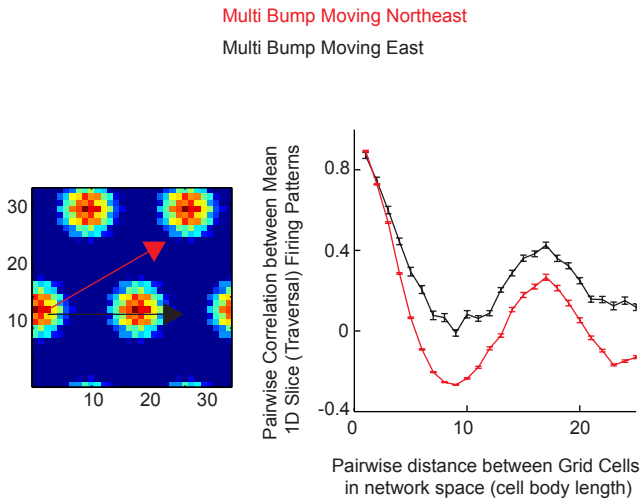

B

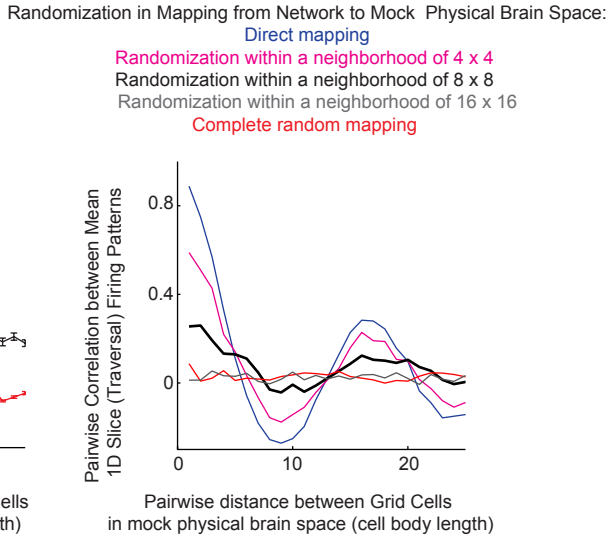

C

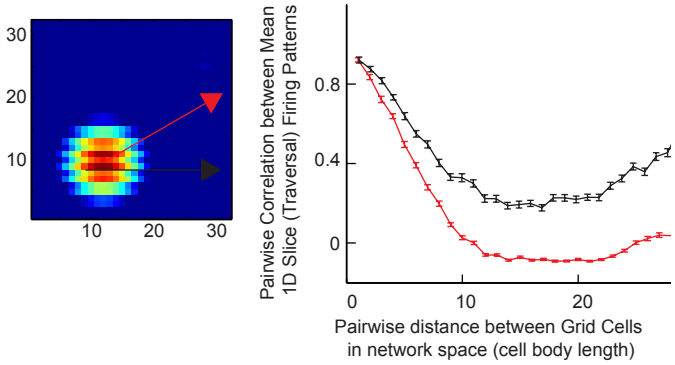

Supplemental Figures

Figure S1, related to Figure 1 **A.** Epifluorescence image of GCaMP-6f fluorescence through MEC microprism (left), two-photon imaging fields through MEC microprism (middle) and histological sections (post-mortem, right) shown for Mouse 2-5 (Mouse 1 shown in Figure 1). Yellow box on epifluorescence image depicts location of two-photon imaging field and red dot indicates location of Alexa494 pin marking shown in the histological section. Sagittal histological sections (identified from pin marking, red) show imaging locations (yellow bar), GCaMP-6f labeled neurons in MEC (green) and morphology from DAPi staining (blue). The characteristic shape of the hippocampus at the medial-lateral position of the sagittal sections indicates recordings were made in MEC. Histological sections for mouse 2 show sagittal sections at location of pin mark (top) and location of 2 photon imaging field (bottom). **B.** Histograms of the number of significant calcium transients per cell per 10,000 frames across all cells (left), grid cells (middle) and non-grid cells (right). **C.** Histograms of the maximum amplitude of each significant calcium transient across all cells (left), grid cells (middle) and non-grid cells (right). **D.** Histograms of the duration of each significant calcium transient across all cells (left), grid cells (middle) and non-grid cells (right). **E.** Triggered average of the smallest 3% of statistically significant somatic Ca^{2+} transients.

Figure S2, related to Figure 2. Additional properties of optically recorded grid cells. **A.** Field of layer 2 MEC neurons labeled with GCaMP-6f and imaged through MEC microprism with two-photon microscopy sequentially on the same day in 2 different environments. In this example, the same grid cells (C1-C8) were recorded on a 6 meter track (top) and a 3 meter track (bottom). **B.** Mean track firing patterns for the 8 grid cells shown in **A** on the 6 meter and 3 meter tracks.

C. As expected for grid cells, a greater number of grid fields were seen in the long versus short track ($P < 0.01$, $n = 24$, Student's t-test), and a similar width of grid fields was seen across the two tracks ($P = 0.88$, $n = 24$, Student's t-test). **D.** In order to compare grid field widths and number of grid fields per meter along the dorsal-ventral axis, each imaging field was divided into a dorsal and a ventral half. The mean distance between the dorsal and ventral half fields was 159 ± 15 μm (n = 16 imaging fields). Over this range of dorsal-ventral recordings, previous data from electrophysiological recordings in mice (Giocomo et al., 2011) would suggest that there would be at most a 7.7% increase in grid field spacing, which would be difficult to resolve given the variance in grid field spacing that occurs at a given location. Thus, consistent with electrophysiological data over this spatial range, no significant difference in the number of grid fields per meter (dorsal = 0.5 ± 0.1 fields/m; ventral= 0.5 ± 0.1 fields/m; mean ± STD; $n = 16$, $P = 0.78$, Student's t-test) or in the grid field widths (dorsal = 44 ± 8 cm; ventral = 43 ± 3 cm; mean ± STD; $n = 16$, $P = 0.69$, Student's t-test) was observed between grid cells in the dorsal versus ventral half fields. **E.** The fraction of neurons classified as grid cells was not significantly correlated with imaging depth over the limited range explored in this study ($P = 0.84$, $\rho = 0.0566$, Spearman Rank Correlation Coefficient). **F.** mean and STD reported for grid field width recorded while rats ran a 3 meter track in a real environment using tetrodes (dark blue, (Hafting et al., 2008)), recorded while rats ran on a 18 meter track in a real environment using tetrodes (green, (Brun et al., 2008)), recorded while mice ran on a 4 to 8 meter virtual track using tetrodes (red, (Domnisoru et al., 2013)), recorded while mice ran on a 4 to 8 meter virtual track using intracellular electrodes (yellow, (Domnisoru et al., 2013)) and while mice ran on a 4 or 5 meter track using 2 photon imaging of GCaMP-6f (light blue, present data). **G.** mean and STD reported for number of grid fields per meter recorded while rats ran a 3 meter track in a real environment

using tetrodes (dark blue, (Hafting et al., 2008)), recorded while rats ran on a 18 meter track in a real environment using tetrodes (green, (Brun et al., 2008)), recorded while mice ran on a 4 to 8 meter virtual track using tetrodes (red, (Domnisoru et al., 2013)), recorded while mice ran on a 4 to 8 meter virtual track using intracellular electrodes (yellow, (Domnisoru et al., 2013)) and while mice ran on a 4 or 5 meter track using 2 photon imaging of GCaMP-6f (light blue, present data).

Figure S3, related to Figure 2. GCaMP-6f ΔF/F versus linear track position traces for 20 grid cells recorded from 3 mice (grid cells 1-8 are from mouse 1, grid cells 9-14 from mouse 2 and grid cells 15-20 from mouse 3). Each of the track traversals is shown for each of the 20 grid cells (bottom, significant transients highlighted in red) along with the mean of ΔF/F versus track position for all traversals (top). Significant grid fields highlighted in green.

Figure S4, related to Figure 4. Pairwise mean track firing correlations versus distance. **A.** Plot of mean grid cell-grid cell distance versus mean track firing pattern correlation averaged over all grid cells in all acquired time-series (black). Same plot is also shown for all non-grid cells from the same acquired time-series (blue). Thick dark line represents moving average (30 micron window) with light bands depicting SEM. Thin dark line represents mean of data binned at 10 micron increments. Grid cell versus non-grid cell profiles are significantly different ($P < 10^{-12}$, Kolmogorov–Smirnov test) **B.** Mean track firing pattern correlation for grid cell (black) and non-grid cell (blue) populations separated by 20-50 μm, 111-147 μm, and 200-256 μm. Grid cell comparisons: $P < 0.01$, One-way ANOVA; ** indicates $P < 0.01$, Post-hoc Tukey-Kramer. Non-grid cell comparisons: $P < 0.01$, One-way ANOVA; ** indicates $P < 0.01$, N.S. indicates $P > 0.05$, Post-hoc Tukey-Kramer. **C.** Plot of mean grid cell-grid cell distance versus mean track

firing pattern correlation averaged over all grid cells in all acquired time-series measured in the dorsal-ventral dimension (magenta). Same plot is also shown for a randomized data set in which grid cells were left in the same location but were randomly assigned the mean track firing pattern of a different grid cell (red). Thick dark line represents moving average (30 micron window) with light bands depicting SEM. The experimental data profile (magenta) was found to be statistically significantly different than the randomized data profile (red) ($P < 10^{-19}$, Kolmogorov–Smirnov test) (** and * indicate $P < 0.01$ and $P < 0.05$ respectively, Bootstrap P-value, from comparison to randomized data). **D.** Plot of mean grid cell-grid cell distance versus mean track firing pattern correlation averaged over all grid cells in all acquired time-series measured in the medial-lateral dimension (green). Same plot is also shown for a randomized data set in which grid cells were left in the same location but were randomly assigned the mean track firing pattern of a different grid cell (red). Thick dark line represents moving average (30 micron window) with light bands depicting SEM. The experimental data profile (green) was found to be statistically significantly different than the randomized data profile (red) ($P < 10^{-25}$, Kolmogorov–Smirnov test) (** and * indicate $P < 0.01$ and $P < 0.05$ respectively, Bootstrap P-value, from comparison to randomized data).

Figure S5, related to Figure 4 Grid cell - Grid cell pairwise 1D slice (traversal) firing pattern correlation is a monotonically increasing function of 2D phase similarity. **A.** Environment firing pattern of 4 grid cells (black, red, blue and green) with different spatial phases. **B.** Mean spatial firing pattern of 4 grid cells shown in **A** generated from an on-axis slice (traversal) (bottom) and off-axis slice (traversal) (top). **C.** Pairwise correlation of the mean slice (traversal) firing pattern

versus relative grid field phase computed for 8 grid cells relative to grid cell 1, shown for an on-axis slice (traversal) (black) and 3 off-axis slices (traversals) (grey, yellow and magenta).

Figure S6, related to Figure 4. CAN grid cell models used to generate a Mexican Hat shaped relationship between grid cell-grid cell distance and environment firing pattern correlation. **A.** Simulation of a multi-bump network with activity bumps moving East (black, i.e. 1D slice/traversal) or Northeast (red; i.e. 1D slice/traversal) across the network (left) generates a Mexican Hat shaped relationship between pairwise environment firing pattern correlations and distance between grid cells in network space (right). **B.** Same as A (right), except the position of the grid cells in the network was partially randomized to simulate possible mappings from network space to mock brain space (direct mapping, blue), randomization within a neighborhood of 4 x 4 (magenta), randomization within a neighborhood of 8 x 8 (black), randomization within a neighborhood of 16 x 16. Completely randomized mapping shown in red. **C.** Simulation of a single bump network with activity bump moving East (black, i.e. 1D slice/traversal) or Northeast (red; i.e. 1D slice/traversal) across the network (left) generates a Mexican Hat shaped relationship between pairwise environment firing pattern correlations and distance between grid cells in network space (right).

Supplemental Text

Compared to other methods, our grid cells were on the low end of the range of fields per meter. This could be because our recordings were made at more ventral MEC locations compared to previous studies (Domnisoru et al., 2013; Hafting et al., 2008), or because our imaging methods may be insensitive to many single and double AP events. The latter could lead to missed grid field firing during some field traversals, especially since many grid field traversals along linear

tracks appear to often contain little or no AP firing (Domnisoru et al., 2013; Hafting et al., 2008). Among individual traversals in which a given cell exhibited at least one significant transient, our recordings show ~60% of traversals with firing in only 1 field and ~40% of traversals with firing in more than one field. Similar statistics on single trial data is not readily available from previous publications, making it difficult to compare to our recordings; however the single trial data using our methods appear to be qualitatively similar to many of the raster plots of previous publications (Brun et al., 2008; Domnisoru et al., 2013; Hafting et al., 2008), including many grid cells with little or no AP firing in a given grid field on many traversals and many other grid cells with more consistent grid field firing. Though the grid cell classifier was designed based on recordings using different methods (extracellular tetrode recordings) and possibly from more dorsal regions of the MEC (Domnisoru et al., 2013), it was still used to classify the grid cell population with the assumption that these differences have little effect on grid cell classification; however, more work will be needed to unambiguously classify neurons recorded with imaging methods as grid cells, which may require imaging in open field 2D environments.

Supplemental Methods:

CAN Model Simulations:

Simulation data shown in Figure S6 was generated using the model framework outlined in Burak and Fiete (2009) and publically available at http://people.bu.edu/zilli/gridmodels.html. Parameters were as follows: $\alpha = 50$, $a = 1$, $\lambda = 13$ (for the multi bump model) or $\lambda=23$ (for the single bump model), $\beta = 3/(\lambda^2)$, $\gamma = 1.1x\beta$, spikeThresh = 0.1, dt = 1ms. Simulations were 4000 msec in duration, simulating a constant velocity of (dx/dt; dy/dt) = (0.5; 0) (m/sec). We used a periodic network lattice comprised of 32 x 32 neurons and sampled the activity of 200 randomly selected CAN model grid cells across the network to measure the pairwise correlation between

their 1D slice (traversal) activity patterns versus the distance between them in the network (Figure S6). Distance was computed as the Euclidean distance between neuron's (x,y) coordinates in the 2D network lattice. To simulate mock brain space with completely randomly arranged cell bodies or partially randomly arranged cell bodies (Figure S6B), the dimensions of mock brain space and network space were assumed to be the same. The activity of each cell was first defined in network space (as defined above) and then for mock brain space, blocks of 2 x 2, 4 x 4, 8 x 8, 16 x 16 or 32 x 32 (completely random) cells were defined across the 32 x 32 network and the position of all cells within each block were randomly permuted (these permuted 32 x 32 lattices were defined as mock brain space). For example, for randomization within blocks of 16 x 16, 4 different 16 x 16 blocks were defined (top left, top right, bottom left, bottom right) and the position of all cells in each block was randomly permuted. For each randomization block size, all pairwise correlations between environment activity patterns (for all cell pairs in the 32 x 32 lattice) were then measured versus all pairwise distances between the randomized cell locations in the mock brain space lattice.

Histology:

The surface vasculature seen across the micro-prism was recorded using epifluorescence microscopy (Figure 1, Figure S1A). The location of each two-photon imaging field in MEC layer 2, with respect to the surface vasculature, was then recorded by comparing the surface vasculature patterned observed using two photon microscopy above (caudal to) the imaging field to the previously recorded epifluorescence pattern. Once imaging experiments in each mouse were complete, the mouse was anesthetized with 1-2% isofluorane and the headplate and prism/mount were removed to expose the caudal surface of MEC. A pin coated with Alexa594 was then inserted perpendicular to the caudal MEC surface at an identified region in the vascular

pattern near to the two-photon imaging field locations. The mouse was then euthanized and the brain was removed and fixed in 4% PFA in 0.1M PBS for ~24 hours. The brains were then transferred into a 30% sucrose solution in 0.1M PBS for approximately 2 days until they sank in the solution. The tissue was sectioned in 100 micron sagittal slices using a freezing microtome. Free floating slices were then incubated for 1 hour in a 70 μM DAPi solution in DDH_20. MEC was identified based on the shape of the cell body layers in the hippocampus. Two photon imaging fields were then confirmed to be located in the identified MEC regions based on known distances from the pin mark sites (Figure 1, Figure S1A).